# ORCA – Online Research @ Cardiff

Citation for final published version:

Li, Simin, Ceccato, Marcel, Lu, Xiuyuan, Frank, Sara, Lock, Nina, Roldan, Alberto, Hu, Xin-Ming, Skrydstrup, Troels and Daasbjerg, Kim 2021. Incorporation of nickel single atoms into carbon paper as self-standing electrocatalyst for CO2 reduction. Journal of Materials Chemistry A: materials for energy and sustainability 9 , pp. 1583-1592. 10.1039/D0TA08433F

Publishers page: http://dx.doi.org/10.1039/D0TA08433F

# Incorporation of nickel single atoms into carbon paper as self-standing electrocatalyst for $CO_2$ reduction

Simin Li[a], Marcel Ceccato[a], Xiuyuan Lu[b], Sara Frank[a], Nina Lock[c], Alberto Roldan[b], Xin-Ming Hu[a,d,*], Troels Skrydstrup[a], and Kim Daasbjerg[a,*]

The design of selective and efficient catalysts for electrochemical $CO_2$ reduction is highly desirable yet still challenging, in particular, if the aim is to make them binder-free and self-standing. Here, we report a new and straightforward strategy to incorporate Ni single atoms into a commercially available carbon paper to prepare a self-standing electrode. This is accomplished by consecutive acid activation, adsorption of $Ni^{2+}$ ions, and pyrolysis steps. Structural characterizations and calculations based on density functional theory consistently suggest that the Ni single atoms are coordinated with three N and one S atoms on the carbon paper. When used for $CO_2$ electroreduction, the electrode exhibits an optimal selectivity (91%), activity (3.4 mA $cm^{-2}$), and stability (at least 14 h) for CO production in water at an overpotential of 660 mV. This report may inspire the design and incorporation of single atoms of various metal types into carbon papers, or other kinds of carbon substrates, for a wide range of electrocatalytic processes.

## Introduction

There is a pressing need to advance technologies of $CO_2$ capture and utilization because of the increasing consumption of fossil fuels and the overproduction of $CO_2$.[1, 2] Electrochemical $CO_2$ reduction reaction (*e*$CO_2$RR) offers a promising way to manage the $CO_2$ balance under ambient conditions and generate valuable chemical commodities at the same time.[3, 4] However, many challenges still remain before achieving high efficiency conversion due to the inert nature of $CO_2$.[5] Furthermore, the hydrogen evolution reaction (HER) is kinetically more favorable and therefore competes with *e*$CO_2$RR in aqueous media.[6, 7] To overcome these problems, electrocatalysts with high selectivity and efficiency are highly demanded.[6, 8]

Molecular catalysts, such as metal-multipyridine and metal-porphyrin complexes, have shown impressive activity and selectivity to catalyze $CO_2$ reduction to CO in water when they are immobilized on electrodes with the assistance of porous carbon materials[9-11] or by incorporation into three-dimensional frameworks.[12-14] With structures resembling metal porphyrins, atomic metal sites directly embedded in carbon materials have been widely developed and have exhibited activity and selectivity comparable to those of immobilized molecular catalysts.[15-19] Both types of catalysts, being in the powder form, usually need to be pasted onto an electrode support surface before utilization. For this purpose, Nafion, a commonly used external binder material is required because the powder catalysts alone bear insufficient adherence onto electrode surfaces.[20] Unfortunately, catalyst detachment during *e*$CO_2$RR due to the gas evolution, is often seen for such electrodes, in particular at high current density. Furthermore, the Nafion binder may provide an insufficient electrical conductivity that limits the electron transfer at the interface of the electrode/catalyst particles and between the particles themselves.

To solve the issues caused by powder catalysts, researchers have resorted to self-standing electrodes. For example, molecular catalysts have been grafted onto electrode surfaces through robust chemical bonding.[21-23] Unfortunately, the resulting electrodes generally exhibit poor activity and/or selectivity due to the low concentration of grafted catalysts.[24] Efforts to make self-standing electrodes with atomic metal sites embedded are rare. Recently, one example was reported by He and co-workers on the preparation of single-atom nickel-decorated porous carbon membranes.[25] Unfortunately, the preparation method requires the pre-synthesis of a metal-organic framework used as a template and, in addition, it employs a specialized electrospinning equipment.

For many powder-based catalysts, carbon paper (CP) is used as a support and current collector for various electrochemical reactions (e.g. oxygen reduction, oxygen evolution, HER, *e*$CO_2$RR etc.) thanks to its high electrical conductivity and mechanical strength.[26] While CP itself is catalytically inactive,[27, 28] activity can be achieved by building-in active sites. In this work, we report the incorporation of atomic Ni into a commercially available CP, which can act as a self-standing electrode for efficient $CO_2$ reduction. The preparation of this electrode was achieved by successive acid activation, $Ni^{2+}$ ions adsorption, and pyrolysis in the presence of a nitrogen source. These steps were all found to be required to make a CP self-standing electrode with optimal activity, selectivity, and stability for $CO_2$-to-CO conversion in water.

## Experimental Section

### Chemicals and Synthesis

**Chemicals**. All chemicals are commercially available and used without further treatment. Concentrated sulfuric acid (98% $H_2SO_4$), concentrated nitric acid (68% $HNO_3$), nickel (Ⅱ) nitrate hexahydrate [$Ni(NO_3)_2 \cdot 6H_2O$], and urea were purchased from Sigma-Aldrich. Carbon paper (CP), Toray 060 pretreated with PTFE and AvCarb MGL 190 that is F-free, was from Fuel-Cell-Store.

**Preparation of ACP/S-N-Ni.** The raw CP was cut into small pieces with a size of 1 cm × 2.5 cm each, which was cleaned using sonication in Milli-Q water and acetone for 15 min, respectively. For the acid activation, an area of 1 × 1 cm$^2$ of the CP was immersed into a solution mixture of 45 mL 98% $H_2SO_4$ and 15 mL 68% $HNO_3$ for 2 h at room temperature under stirring. Subsequently, the CP pieces were washed with Milli-Q water at least five times to remove acid residues and dried in the fume hood to obtain activated CP (ACP). The ACP with the same activated area of 1 × 1 cm$^2$ was then immersed into 3.0 mg mL$^{-1}$ $Ni(NO_3)_2{\cdot}6H_2O$ solution for 15 h at room temperature under stirring. ACP-Ni$^{2+}$ was obtained by washing with Milli-Q water at least five times to remove Ni$^{2+}$ residues and dried in the fume hood. In the pyrolysis step, ACP-Ni$^{2+}$ and 0.20 g urea were placed in separate quartz boat, which was put in a tubular furnace (urea was 1.5 cm away from ACP-Ni$^{2+}$ in the upstream). The furnace was heated up to 800 °C at a heating rate of 10 °C min$^{-1}$ and kept at 800 °C for 1 h under Ar atmosphere to obtain ACP/S-N-Ni. The furnace was allowed to cool down to room temperature.

**Preparation of ACP/S.** ACP/S was prepared directly from pyrolysis of ACP under the same conditions as for ACP/S-N-Ni, the only difference being that no Ni$^{2+}$ was pre-adsorbed and no urea was used.

**Preparation of ACP/S-N.** ACP/S-N was produced by pyrolyzing ACP in the presence of urea under the same conditions as for ACP/S-N-Ni, the only difference being that no Ni$^{2+}$ was pre-adsorbed.

**Preparation of ACP/S-Ni.** ACP/S-Ni was obtained by pyrolyzing ACP-Ni$^{2+}$ at the same conditions as for ACP/S-N-Ni, the only difference being that no urea was used.

**Preparation of CP/N-Ni.** The raw CP was directly used for Ni$^{2+}$ adsorption and pyrolysis under the same conditions as for ACP/S-N-Ni. No acid activation step was performed.

### Characterizations of Materials

**Powder X-ray diffraction (PXRD).** PXRD data was obtained from a Rigaku SmartLab X-ray diffractometer using monochromatic Cu K$\alpha_1$ radiation ($\lambda$ = 1.54056 Å) and a D/texUltra1D detector. The diffraction patterns were recorded with the $2\theta$ window set from 5–90° (step size of 0.04° and a scan rate of 0.1° s$^{-1}$).

**Inductively coupled plasma - optical emission spectroscopy (ICP-OES).** The Ni content in the electrode was measured on an Agilent 5110 ICP-OES equipment with an RF power of 1.20 KW. A piece of the as-prepared self-standing electrode with an area of 1 × 0.5 cm$^2$ was ground into powder before the measurement.

**Raman spectroscopy.** Renishaw inVia confocal Raman microscope was utilized to record Raman spectra. An Ar-ion laser excitation at 514 nm was used with 5 mW power. A grafting monochromator with 1200 lines mm$^{-1}$ was mounted and point-by-point mapping was given with 4 × 4 points separated by a distance of 3 µm. For each material, three maps at different locations were averaged and analyzed to give the overall spectrum.

**X-ray photoelectron spectroscopy (XPS).** XPS analysis was performed on a Kratos Axis Ultra-DLD instrument using a monochromatic Al Kα X-ray source at 150 W. The pressure was kept below 5×10$^{-9}$ mbar during the measurements. The full survey spectra were obtained with a pass energy of 160 eV and the high-resolution spectra of C 1s, O 1s, N 1s, S 2p, and Ni 2p with 20 eV. The CasaXPS software was used for fitting and all spectra were calibrated with C 1s binding energy setting of 284.5 eV.

**X-ray absorption spectroscopy (XAS).** XAS measurements were performed at beamline B18 at the Diamond Light Source. The data was collected in continuous scan mode where ACP/S-N-Ni and NiTPP were measured on a Ge 36 element detector in fluorescence mode. The scan time was ~160 s and 3–6 scans were collected for each sample to improve statistics. The scan range was from −200 to 850 eV relative to the *K* absorption edge for Ni. The resulting data were processed in Athena and the data fitting data was conducted in Artemis.[29]

**Scanning electron microscopy (SEM).** SEM images of CP-based materials were acquired on an FEI Nova 600 instrument equipped with a through-the-lens detector at 5 kV accelerating voltage. High-vacuum conditions and imaging in immersion mode were used.

**Transmission electron microscopy (TEM).** TEM characterization was performed at 200 kV with a TALOS F200A transmission electron microscope equipped with a TWIN lens system, an X-FEG electron source, and a Ceta 16M Camera. Bright-field images were acquired in TEM mode, and the elemental analysis was done by using energy-dispersive X-ray spectroscopy (EDS) mapping acquired in STEM mode. Aberration-corrected high-angle annular dark-field scanning transmission electron microscopy (HAADF-STEM) images were acquired on the JEM-ARM200F instrument at 200 keV. In the particular case of measurements on ACP/S-N-Ni, this material was peeled off using strong sonication in absolute ethanol for 2 h. Some of the carbon material from the upper surface was then uniformly dispersed in absolute ethanol. Four drops of the suspension were deposited on a lacey carbon-supported Cu grid (300 mesh).

### *e*CO$_2$RR

A three-electrode system was employed for all electrochemical studies. The as-prepared CPs were directly used as working electrodes with an active geometric area of 1 × 1 cm$^2$. A platinum mesh served as a counter electrode and the reference was a leak-free Ag/AgCl electrode (ElectroCell LF-1). The relationship between the reversible hydrogen electrode (RHE) and the Ag/AgCl electrode is given by eq (1).

$$E\text{ (vs RHE)} = E\text{ (vs Ag/AgCl)} + 0.197\text{ V} + RT/F \times \ln 10 \times \text{pH} \qquad (1)$$

In this expression, $R$ denotes the gas constant, $T$ is the temperature, and $F$ is Faraday´s constant. The electrolyte used was 0.5 M $KHCO_3$ with pH = 7.3 under saturation with $CO_2$ and pH = 8.4 under saturation with Ar.

**Cyclic Voltammetry.** Cyclic voltammetric experiments were carried out on a CHI 601D potentiostat connected to the three-electrode setup.

**Controlled-Potential Electrolysis and Gas Quantification.** Controlled potential electrolysis was recorded in an H-cell using a CHI 601D potentiostat. The cathodic and anodic chambers were separated by a glass frit. The cathodic chamber contained the as-prepared self-standing electrode as a working electrode and a Ag/AgCl reference electrode, while the anodic chamber had a platinum mesh as a counter electrode.

For the 15 min electrolysis, carried out at room temperature and under ambient pressure, the electrolyte was first purged with $CO_2$ for 15 min under stirring. Subsequently, amperometric curves were recorded at varying potentials. In the poisoning experiment, 10 mM KCN was added to the cathodic electrolyte. After each electrolysis, 250 µL gas from the headspace (total volume = 51 mL) was injected into an Agilent Technologies 7890B gas chromatography (GC). The GC was equipped with a thermal conductivity detector (TCD). The gas mixture was separated by the Agilent Select Permanent Gases. Ar was utilized as the gas carrier (14 mL $min^{-1}$), the oven was set at 45 °C and the TCD temperature was at 200 °C.

For long-term electrolysis (14 h), the electrolyte was also first purged with $CO_2$ for 15 min. During electrolysis, $CO_2$ was continuously supplied to the cathodic solution at a constant flow of 10 mL $min^{-1}$ at room temperature and under ambient pressure. The gas products produced were automatically sampled to the GC system every 30 min.

The faradaic efficiency (FE) can be calculated according to eq (2).[18]

$$\mathrm{FE}_x = \frac{v f_x P F \alpha}{R T i} 100\% \qquad (2)$$

where $x$ is the specific gas product, CO or $H_2$, $v$ is the $CO_2$ flow rate, $f_x$ denotes the volume concentration of CO or $H_2$ in the gas flow delivered to the gas chromatograph at a given sampling time, $P$ is the ambient pressure (= $1.01 \times 10^5$ Pa), $F$ is the Faraday constant (= 96485 C $mol^{-1}$), $\alpha$ is the number of electrons for $CO_2$-to-CO or water-to-$H_2$ conversion (= 2 for both cases), $R$ is the gas constant (=8.314 J $mol^{-1}$ $K^{-1}$), $T$ = 296 K, and $i$ denotes the current at the given time.

The turnover frequency (TOF) for the $CO_2$-to-CO conversion is calculated from eq (3).[30]

$$\mathrm{TOF} = \frac{|j| \times FE_{CO}}{\alpha \times F \times C_{Ni}} \qquad (3)$$

where $j$ is the current density and $C_{Ni}$ is the molar concentration of Ni single atoms in the electrode determined by ICP-OES.

**Calculation details**

All DFT calculations were conducted using the Vienna Ab-initio Simulation Package (VASP).[31, 32] The Perdew-Burke-Ernzerhof (PBE) method of the generalized gradient approximation (GGA)[33] was adopted as the term exchange correlation with a kinetic cut-off energy of 450 eV. Furthermore, the effect of the inner core in the modelling was represented by the projector augmented wave (PAW).[33] Optimized structures were converged within a threshold of internal forces smaller than 0.01 eV $Å^{-1}$ with the conjugate gradient algorithm and an electronic relaxation threshold of $10^{-5}$ eV.

The optimized lattice parameter of graphene is 2.470 Å, which agrees well with the expected value of 2.464 Å.[34] The surfaces were represented by a p(4 × 4) supercell slab with a separation between active sites of 9.88 Å. The Brillouin zone was sampled by a 0.2 $Å^{-1}$ *k*-spacing grid with Methfessel-Paxton smearing broadening of $\sigma$ = 0.2 eV to acquire an accurate description of the total energy. A vacuum of 15 Å was added perpendicularly to the surface to avoid spurious interaction with periodic images.

We used the energy of pristine graphene, nitrogen molecule, P2/c sulfur, and fcc nickel bulk (lattice = 1.743 Å) as reference to calculate the formation energies of the doped surface according to eq (4).

$$E_{\mathrm{formation}} = E_{\mathrm{surf}} - \sum_i n_i * E_{\mathrm{atomic}} \qquad (4)$$

The parameter $E_{\mathrm{surf}}$ is the energy of doped surfaces, $i$ is the species of atoms, including C, N, S, and Ni, and $E_{\mathrm{atomic}}$ is the atomic energy of reference (see **Table S1**).

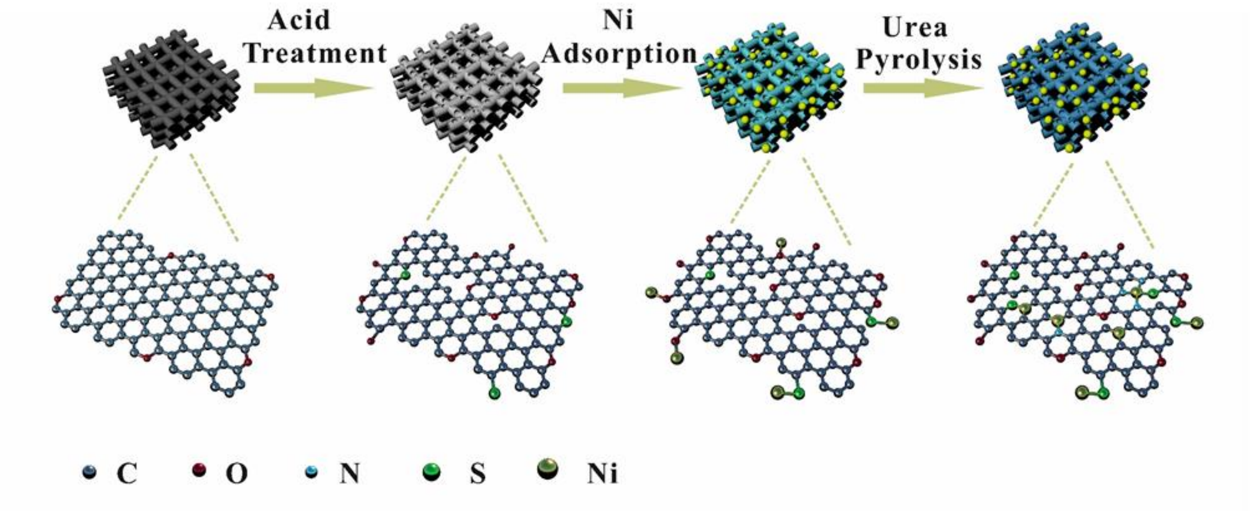

**Figure 1**. Protocol for preparation of ACP/S-N-Ni.

The adsorption energy of intermediates in the reactions is defined by eq (5).

$$E_{\mathrm{ads}} = E_{\mathrm{system}} - E_{\mathrm{surface}} - E_{\mathrm{molecule}} \qquad (5)$$

The parameter $E_{\mathrm{system}}$ is the total energy of the adsorbed system, and $E_{\mathrm{surface}}$ and $E_{\mathrm{molecule}}$ denote the energy of clean surface and adsorbate in the gas phase, respectively. For the reaction steps containing pairs of proton and electron transfer, the relative free energies were calculated based on the computational hydrogen electrode (RHE) model, where the chemical potential of a pair of proton and electron ($H^+$ + $e^-$) is referred to as a $H_2$ molecule.[35] The difference in energy was calculated by the electronic energy obtained from the DFT calculation.

## Results and Discussion

### Synthesis and Characterization

**Figure 1** outlines the protocol for the preparation of the self-standing electrode containing single Ni atoms (denoted ACP/S-N-Ni, where ACP stands for activated carbon paper, and S, N, and Ni are the doping atoms therein). It includes three successive steps, i.e. (1) activation of CP, (2) adsorption of $Ni^{2+}$ ions on the activated CP, and (3) pyrolysis of the CP material in the presence of urea. Raman spectroscopy and X-ray photoelectron spectroscopy (XPS) were used to monitor the chemical changes induced by each of these steps to the CP.

In the activation step, the commercial fluoridized CP is treated in a concentrated $H_2SO_4$-$HNO_3$ mixture, leaving a substantial number of defects and oxygenate functional groups on the resultant ACP. The successful introduction of defects on ACP is supported by Raman spectroscopy, which presents a large defect (D) peak as compared to the pristine CP (**Figure 2a**). The creation of additional oxygenate species on the ACP surface is verified by XPS, where a much stronger O peak is observed (**Figure 2b** and **Table S2**). Meanwhile, the emergence of a small S signal is evident in the XPS survey while the high-resolution spectrum shows the attachment of sulfonic acid groups (**Figure 2b,c** and **Table S2**). In fact, deconvolution of C 1s and O 1s core-level spectra reveals that the oxygen functionalities are hydroxyl, carbonyl, carboxyl, and sulfonic acid groups (**Figure S1**). Note that the strong F 1s signal originates from the as-received CP (treated with polytetrafluoroethylene).

The subsequent $Ni^{2+}$ adsorption to form ACP-$Ni^{2+}$ is expected to take place smoothly by immersing the ACP in aqueous $Ni^{2+}$ solution. This is due to the fact that the previously formed defects and oxygenates provide abundant sites to effectively coordinate to $Ni^{2+}$ ions.[36, 37] Unfortunately, the adsorption of $Ni^{2+}$ is not observable in the XPS spectra (**Figures 2b,c** and **S1**) since the Ni 2p peak is overshadowed by the F 1s peak from the polytetrafluoroethylene treated CP.

Finally, the self-standing ACP/S-N-Ni electrode is produced by pyrolysis of ACP-$Ni^{2+}$ at 800 °C under argon atmosphere in the presence of urea. The urea serves as a source of nitrogen atoms intended to stabilize the single Ni atoms through coordination together with the existing S atoms. By doing so, a Ni loading up to 1.04 wt% was achieved in ACP/S-N-Ni, as determined by ICP-OES (**Table S3**). XPS shows the incorporation of both Ni, N, and S atoms with the S species changing from sulfonic to mainly thienyl type with a small amount of Ni-S species (**Figure 2c,d**). In addition, F atoms are completely removed from ACP/S-N-Ni, as F 1s (or C 1s) from the $CF_2$ signal is no longer observed in XPS (**Figures 2b** and **S1**). The Ni 2p spectrum of ACP/S-N-Ni shows a binding energy (855.6 eV) slightly larger than that of $Ni^{2+}$ (855.2 eV) in nickel tetraphenylporphyrin (NiTPP) (**Figure 2e**). This noticeable shift to higher energies indicates a valence state of >2+ of Ni in the electrode, which could be ascribed to the decrease in electron density at the Ni sites because of electron transfer to the adjacent electron-withdrawing functionalities (oxidized N and S).[38] No metallic $Ni^0$ characterized by a binding energy of 853.6 eV is detected in ACP/S-N-Ni.[39, 40] The N can be deconvoluted into five species, including pyridinic, pyrrolic, graphitic, oxidized, and Ni-coordinated N species. The Ni-N bonding indicates the presence of isolated Ni atoms

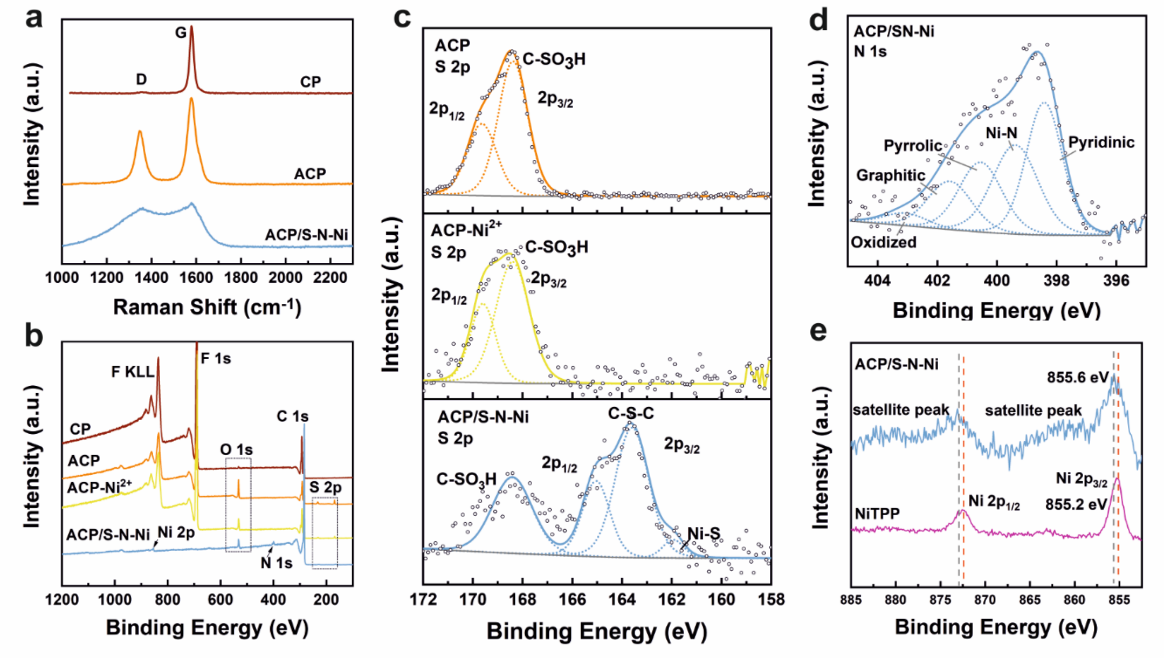

**Figure 2**. (a) Raman spectra of CP, ACP, and ACP/S-N-Ni along with (b) XPS survey and (c) S 2p spectra of CP and ACP, ACP-Ni$^{2+}$, and ACP/S-N-Ni. (d) N 1s and (e) Ni 2p XPS spectra of ACP/S-N-Ni.

coordinated with N atoms. In addition, the incorporation of Ni and N atoms in ACP/S-N-Ni disrupts the original graphitic structure of ACP and gives rise to a higher degree of disorder, as evidenced from the almost similar intensity observed of the two broad D and G bands in Raman (**Figure 2a**).[41]

For comparative purposes, we performed a series of control experiments involving CP electrodes synthesized to contain only S (ACP/S), S and N (ACP/S-N), S and Ni (ACP/S-Ni), and N and Ni on non-activated CP (CP/N-Ni) as described in the Experimental Section. Unsurprisingly, XPS shows that ACP/S and ACP/S-N synthesized without the pre-adsorption step of Ni$^{2+}$ contain no Ni (**Figures S2** and **S3**, **Table S2**). In contrast, ACP/S-Ni contains Ni, but still much less than ACP/S-N-Ni which we attribute to the reduced ability of S alone to coordinate with Ni atoms. In the case of CP/N-Ni, exposed to pre-adsorption of Ni and pyrolysis in the presence of urea but with no prior acid treatment of CP, one sees no Ni. We attribute this to the lack of oxygenates in the untreated CP for accomplishing an effective adsorption of Ni$^{2+}$, thus substantiating the importance of the acid treatment for the incorporation of Ni atoms in self-standing CP electrodes.

Synchrotron-based X-ray absorption spectroscopy (XAS) was utilized to uncover the electronic configuration and coordination environment of Ni atoms in ACP/S-N-Ni. **Figure 3a** displays the Ni K-edge X-ray absorption near-edge spectra (XANES) of the ACP/S-N-Ni electrode and two reference materials, i.e. NiTPP and Ni foil. The pre-edge position is determined by the inflection point in the rising-edge region of the second-derivative spectra.[8] ACP/S-N-Ni has a pre-edge position of 8338.8 eV, slightly larger than that of NiTPP (8337.8 eV) and much larger than that of the Ni foil (8333.0 eV, inset in **Figure 3a**). Notably, the intensity of the white line of ACP/S-N-Ni is between those of NiTPP and Ni foil. All in all, this suggests that the Ni oxidation state in ACP/S-N-Ni is slightly larger than 2+, in good agreement with the XPS results.

**Figure 3b** shows the Fourier transform of the Ni K-edge phase-uncorrected extended X-ray absorption fine structure (EXAFS) of ACP/S-N-Ni, NiTPP, and Ni foil. For ACP/S-N-Ni ($k^3$-weighted $k$-space spectra before Fourier transform is shown in **Figure S4**), a dominant peak is at $R$ = 1.77 Å, which is larger than the 1.53 Å found for the Ni-N$_4$ coordination in NiTPP[8] and the 2.18 Å for the Ni-Ni bonding in the Ni foil. These results exclude the presence of metallic Ni$^0$ in ACP/S-N-Ni and point to the possibility that Ni is coordinated with S, in addition to N, thus showing a larger $R$ position. To substantiate this, density functional theory (DFT) calculations were used to explore six possible first-shell structures hosting Ni atoms on the basis of their formation energy and electronic configuration (**Figures 3c** and **S5, Table S1**). The calculations support the conclusion that the structure with Ni coordinated to three N and one S atoms (N$_3$S–Ni) fits the experimental EXAFS data best (**Table S1**).

Scanning electron microscopy (SEM) shows that the morphology of ACP/S-N-Ni is similar to that of raw CP (**Figure S6**). This suggests that the acid activation and subsequent pyrolysis do not change the macroscopic structure of CP. To get to the microscale structures, we peeled off the top layers of ACP/S-N-Ni using intensive sonication in absolute ethanol. The appertaining images recorded by transmission electron microscopy (TEM) reveal that ACP/S-N-Ni contains nanoscale graphitic sheets on its surface (**Figure 4a**). This is in line with its X-ray diffraction (XRD) pattern, where a strong diffraction peak ($2\theta$ = 26°), attributed to graphitic carbon, is seen (**Figure S7**). ACP/S-N-Ni shows a large population of pores having diameters of several nanometers (**Figure 4b**), attributed to defects coming

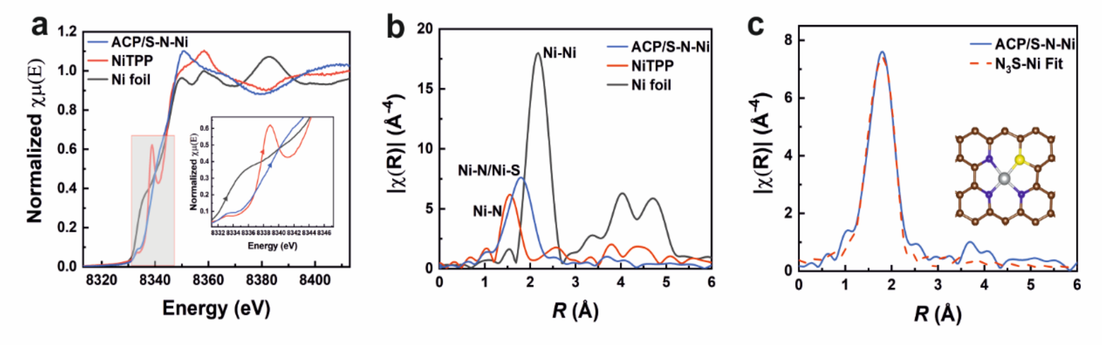

**Figure 3.** (a) Ni K-edge XANES (inset shows enlarged pattern) and (b) Fourier transform of EXAFS spectra of ACP/S-N-Ni and reference materials (i.e. NiTPP and Ni foil). (c) First-shell (N3S-Ni) fitting of the Fourier transform of EXAFS spectra for ACP/S-N-Ni (grey, blue, yellow, and brown spheres represent Ni, N, S, and C atoms, respectively).

from the acid treatment prior to pyrolysis. Importantly, we observe no metallic Ni particles across any of the TEM (**Figure 4a,b**) and the aberration-corrected HAADF-STEM images (**Figure 4c**). The latter clearly shows the existence of abundant and uniformly distributed Ni single atoms in ACP/S-N-Ni. Likewise, the XRD pattern shows no diffraction peaks from crystalline Ni-based particles (**Figure S7**). Finally, the elemental mapping by energy dispersive X-ray spectroscopy (EDS) reveals a homogeneous distribution of Ni, N, and S in the carbon matrix (**Figure 4d**), which, together with the XPS, XAS, and HAADF-STEM characterizations, confirm the atomic dispersion of Ni sites. The uniform distribution of Ni element on a larger scale on the electrode is further confirmed by EDS mapping equipped on SEM (**Figure S6**). Note that the less densely populated S and Ni signals in the blank areas with no ACP/S-N-Ni flakes come from the background noise as usually seen in the elemental mapping of powder materials containing atomic metal sites.[42, 43] Taken together, the successful incorporation of single Ni atoms along with the porosity introduced in the self-standing electrode is expected to offer both efficiency and robustness for the *e*$CO_2$RR.

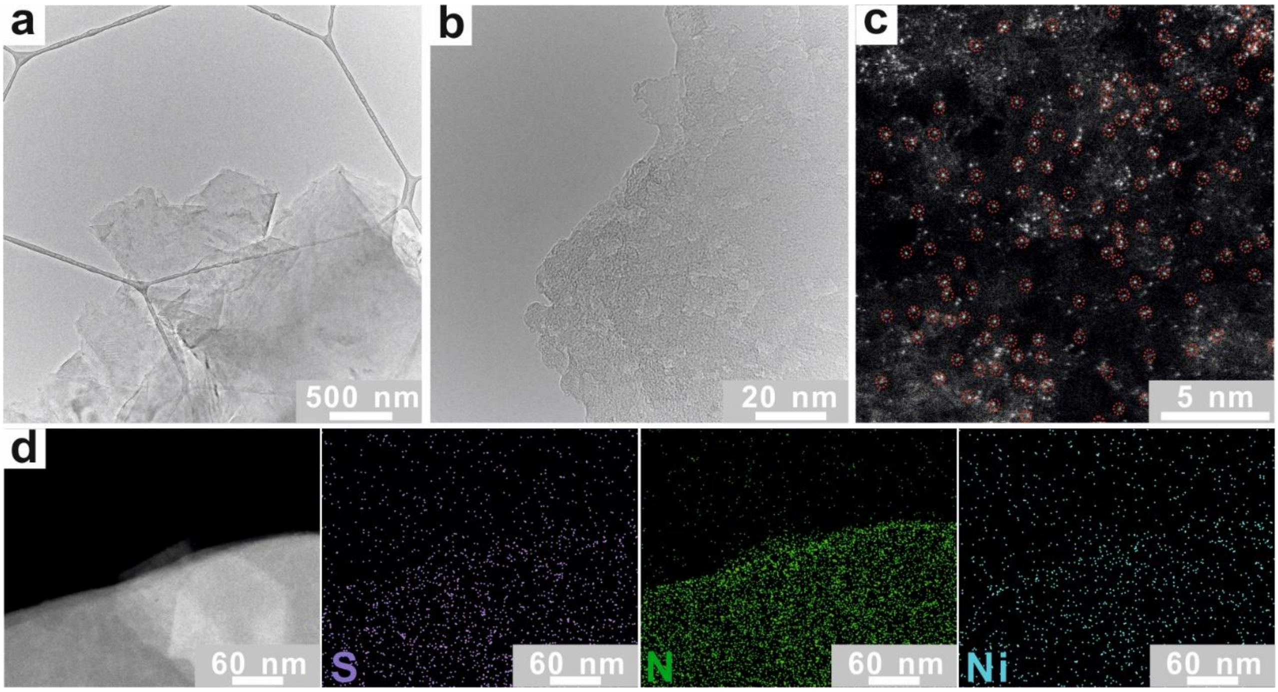

**Figure 4**. (a, b) TEM images and (c) aberration-corrected HAADF-STEM image of flakes peeled off the ACP/S-N-Ni electrode using sonication in absolute ethanol. The Ni single atoms are marked with red circles. (d) STEM images with corresponding elemental mapping.

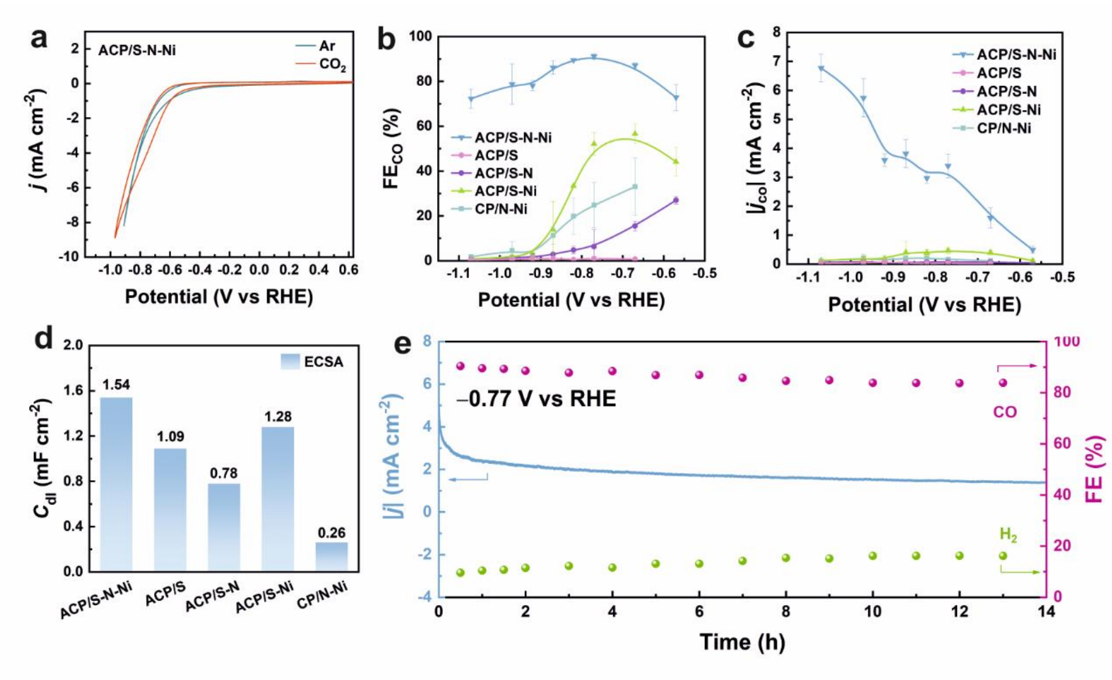

**Figure 5**. (a) Cyclic voltammograms recorded at ACP/S-N-Ni using $v$ = 10 mV s$^{-1}$ under Ar and CO$_2$, respectively. (b) FE$_{CO}$ and (c) $/j_{CO}/$ measured at various potentials for ACP/S-N-Ni, ACP/S, ACP/S-N, ACP/S-Ni, and CP/N-Ni after 15 min electrolysis of CO$_2$. (d) Double layer capacity ($C_{dl}$) of the various electrodes. (e) Recordings of $|j|$ and FE at ACP/S-N-Ni during 14 h electrolysis of CO$_2$. Electrolyte is 0.5 M KHCO$_3$ in all cases.

## *e*CO$_2$RR

**Figure 5a** shows the cyclic voltammograms recorded using ACP/S-N-Ni as the electrode in aqueous 0.5 M KHCO$_3$. Under Ar atmosphere, the reduction current observed is attributed to HER. In the CO$_2$-saturated solution, the reduction current density ($j$) rises dramatically at less negative potential (starting at –0.60 V vs RHE), indicative of an electrocatalytic CO$_2$ reduction. In comparison, all other electrodes (ACP/S, ACP/S-N, ACP/S-Ni, and CP/N-Ni) exhibit smaller $|j|$ under the same conditions and/or show smaller change in current density upon switching from Ar to CO$_2$. This indicates a decreased activity for CO$_2$ reduction on the electrodes used in control experiments (**Figure S8**).

Next, the *e*CO$_2$RR activity was investigated using controlled potential electrolysis at potentials between –1.07 and –0.57 V vs RHE. For all examined electrodes, only CO and H$_2$ were detected by gas chromatography; no products in the electrolyte were observed by $^1$H NMR (**Figure S9**). Starting with the ACP/S electrode, the selectivity for CO$_2$ reduction is exceedingly low with the formation of H$_2$ and almost no CO, independent of potential (**Figure 5b** and **Figure S10a**). Thus, the faradaic efficiency (FE) of CO production, FE$_{CO}$, is essentially zero. In that respect, it helps to incorporate N in the material, affording the ACP/S-N electrode, since this gives a maximum FE$_{CO}$ ≈ 27% at –0.57 V vs RHE. The even more beneficial effect of replacing N with Ni is seen from the significant increase of FE$_{CO}$ to ~57% at –0.67 V vs RHE for ACP/S-Ni. Still, HER becomes dominant at more negative potentials. In any case, the acid treatment during the synthesis of the electrode is crucial for providing abundant oxygenated sites at CP, at which Ni$^{2+}$ ions can effectively adsorb. This becomes evident from the poor performance of the CP/N-Ni electrode with FE$_{CO}$ ≈ 33% at –0.67 V vs RHE. Finally, introducing both Ni and N into an acid-treated CP electrode (i.e. ACP/S-N-Ni) increases FE$_{CO}$ to as much as 91% at –0.77 V vs RHE and with a capability of maintaining >85% in a wide potential range from –0.87 to –0.67 V vs RHE. Note that the maximal FE$_{CO}$ is obtained at a moderate overpotential of 660 mV, given that the equilibrium potential for CO$_2$-to-CO conversion is –0.11 V vs RHE. These results highlight the importance of using N-assisted Ni incorporation into activated CP to make a self-standing selective electrode for CO$_2$ reduction, in line with the observation for powder carbon materials comprising single Ni atoms.[44, 45]

**Figure 5c** shows the absolute value of the partial current density for CO production ($|j_{CO}|$) which is distinctly larger using the ACP/S-N-Ni electrode at all potentials examined, although the total current density (i.e. $|j|$) is of comparable size in all cases because of significant contributions from HER at the other electrodes (**Figure S10b**). Specifically, at the potential with the maximum FE$_{CO}$ achieved, $|j_{CO}|$ = 3.40 mA cm$^{-2}$ for ACP/S-N-Ni (at –0.77 V vs RHE) which is 7.4 times larger than that of the second-best electrode, i.e. ACP/S-Ni with $|j_{CO}|$ = 0.46 mA cm$^{-2}$. At this potential, the mass activity relative to the Ni loading of ACP/S-N-Ni reaches 145 mA mg$^{-1}$, much higher than that of ACP/S-Ni (39 mA mg$^{-1}$) under the same electrolysis conditions (**Figure S11**). This can be further translated to a turnover frequency (TOF) of 0.044 s$^{-1}$ for ACP/S-N-Ni and of 0.012 s$^{-1}$ for ACP/S-Ni, assuming all Ni atoms participate in the eCO$_2$RR. Moreover, while $|j_{CO}|$ for ACP/S-N-Ni continues to increase as

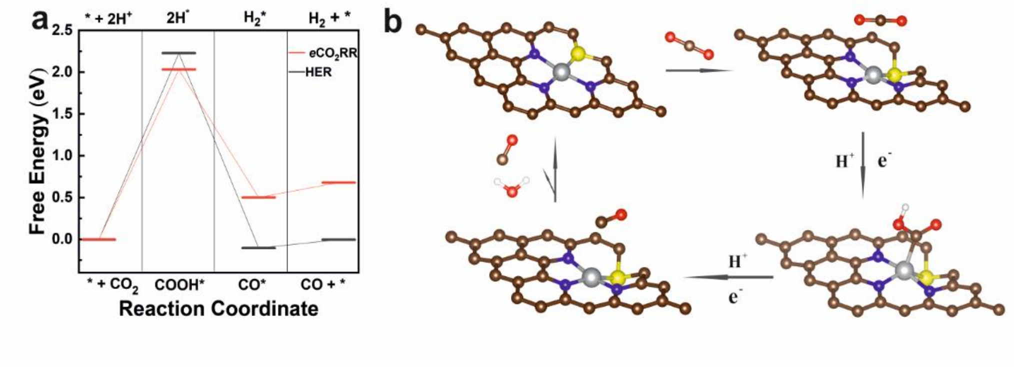

**Figure 6**. (a) Calculated free-energy diagram for *e*$CO_2$RR and HER. (b) Proposed reaction path for $CO_2$ reduction at the $N_3S$-Ni site in the self-standing ACP/S-N-Ni electrode (grey, blue, yellow, brown, red, and white spheres represent Ni, N, S, C, O, and H atoms, respectively).

the potential becomes increasingly negative, $|j_{CO}|$ approaches zero for the other electrodes, thus highlighting the outstanding *e*$CO_2$RR activity of ACP/S-N-Ni.

Concerning the double-layer capacity ($C_{dl}$), the four electrodes treated with an initial acid activation step, i.e. ACP/S-N-Ni, ACP/S, ACP/S-N, and ACP/S-Ni, exhibit larger $C_{dl}$ values than that of CP/N-Ni without initial acid treatment (**Figures 5d**, **S12**, and **S13**). Since $C_{dl}$ is closely related to the electrochemically active surface area (ECSA), we may conclude that the four ACP-based electrodes show larger ECSAs than that of CP/N-Ni. This confirms that the acid activation resulting in the introduction of abundant oxygenates defects induces a larger ECSA after the pyrolysis steps. It should be noted that the relatively smaller differences in the ECSAs of the four ACP electrodes cannot be responsible for the large differences observed in their *e*$CO_2$RR activity. Thus, this would support the conclusion that the high activity of ACP/S-N-Ni originates from its unique active sites.

To confirm that Ni single atoms on the self-standing electrode are indeed the active sites for *e*$CO_2$RR, a poisoning experiment with cyanide ions ($CN^-$) was first performed. Upon introducing 10 mM $CN^-$ to the catholyte, we found that ACP/S-N-Ni exhibited both lowered $FE_{CO}$ and $|j|$ **(Figure S14)**, due to the blocking effect of $CN^-$ toward metal centers.[30, 46, 47] Next, we employed DFT to calculate the relative energy of the key intermediates at the $N_3S$–Ni site (* is used to denote such site) for both the *e*$CO_2$RR and competing HER pathways (**Figure 6a**). In the former case, COOH* is well recognized as being the key intermediate,[48] while H* takes this role in HER.[49] In accordance with this, **Figure 6a** reveals that the formation of COOH*, occurring via the first electron and proton transfer to $CO_2$, has the highest energy barrier to become the rate-limiting step of *e*$CO_2$RR. For the competing HER, the most energy-demanding step is the proton adsorption on the active site via Volmer reaction to form H*.[50] The energy barrier for the first step in *e*$CO_2$RR is lower (2.03 eV) than that for HER (2.23 eV), which explains the high *e*$CO_2$RR selectivity on the $N_3S$–Ni sites at the ACP/S-N-Ni electrode. Once COOH* is formed, the intermediate CO* is exothermically generated in a downhill reaction. Finally, the CO desorption from the site occurs at the cost of a small energy barrier to restore the site for catalysis. **Figure 6b** shows the *e*$CO_2$RR mechanism in greater detail.

Finally, electrolysis was performed at –0.77 V vs RHE for a prolonged period of 14 h with continuous $CO_2$ supply to test the durability of ACP/S-N-Ni (**Figure 5e**). As seen, *j* remains relatively stable over the entire period with the decrease in the absolute value mainly occurring within the first hour. At the same time, $FE_{CO}$ decreases slightly from ~90% to ~84% through the entire electrolysis. XPS spectra of the post-electrolysis ACP/S-N-Ni electrode show negligible changes to the Ni oxidation state and its coordination with N and S, as compared to the pristine ACP/S-N-Ni (**Figure S15**). This attests to the good stability of the self-standing Ni sites for *e*$CO_2$RR.

A final important point to consider is that the ACP/S-N-Ni electrode was prepared from a commercially available and widely used carbon paper that is pretreated with a thin PTFE layer (Toray T-060). To assess the influence of the PTFE layer, we made another self-standing electrode ($F_{free}$-ACP/S-N-Ni) under the same synthesis conditions but now using a PTFE-free carbon paper. For *e*$CO_2$RR, the $F_{free}$-ACP/S-N-Ni electrode exhibits reasonable $FE_{CO}$ and $|j|$, but lower than that of ACP/S-N-Ni (**Figure S16**). This suggests that Ni single atoms can be incorporated into another kind of carbon substrate, but also that the initial presence of the PTFE layer is beneficial for the fabrication of a more active electrode catalyst. Presumably, the depletion of F during the high-temperature preparation process, as observed by XPS (**Figure 2b and S1**), induces more defects on the electrode surface, thus enabling the generation of more active sites.[51]

In general, our self-standing electrode containing single Ni atoms exhibit significantly improved performance in terms of activity and selectivity, compared to similarly chemically bonded metal complex catalysts.[21, 52-56] It can also rival many powder-based single atom catalysts, while avoiding detachment of catalyst materials (**Table S4**).[15, 57] On the other hand, the performance of ACP/S-N-Ni is not competitive with the best state-of-the-art powder-based Ni single atoms, simply because these possess considerably larger ECSAs, as reflected by their tens of times larger $C_{dl}$, to enable better exposure of the active sites (**Table S4**).[58-60] The intrinsically low ECSA of the commercially available carbon paper represents one factor limiting the performance of this kind of self-standing electrodes. Nevertheless, the performance of the electrode could be improved through substrate structure engineering for better exposure of Ni sites.

## Conclusions

In summary, a self-standing electrode containing Ni single atoms was prepared directly from a commercially available carbon paper *via* consecutive acid activation, Ni adsorption, and pyrolysis steps. The electrode can be directly used as catalysts without any other support or binder. The effect of the three synthetic steps (carbon paper activation, $Ni^{2+}$ ions adsorption, and pyrolysis in the presence of urea) are thoroughly studied, and they are all found to be indispensable for achieving an optimum catalytic performance in $e$$CO_2$RR. Activation of the carbon paper introduced abundant defects and functionalities, which helped to effectively adsorb $Ni^{2+}$ ions in the next step. Pyrolysis in the presence of urea trapped and stabilized the Ni single atoms in the target electrode. Multiple characterization techniques reveal that the Ni atoms feature oxidation states of >2+ and are coordinated with three N atoms and one S atom. With such structure, the electrode exhibits high selectivity, activity, and stability for $CO_2$-to-CO conversion in water. This work presents a feasible example of installing Ni single sites into commercially available electrodes and would serve as an inspiration on how to incorporate other single metal sites into carbon paper, or other types of carbon substrates, for a variety of electrocatalytic reactions.

## Conflicts of interest

There are no conflicts to declare.

## Acknowledgements

We thank the Danish National Research Foundation (grant no. DNRF118) for generous financial support. Simin Li (CSC No. 201806370200) and Xiuyuan Lu (CSC No. 201806370221) are financially supported by a PhD scholarship from China Scholarship Council. We acknowledge Diamond Light Source for beamtime, Giannantonio Cibin for experimental support at B18, and DanScatt for financial support. We also acknowledge computing time on the facilities of HPC Wales and the Advanced Research Computing @ Cardiff (ARCCA) at Cardiff University. X.-M. Hu acknowledges the support of Qilu Young Scholars program from Shandong University.

### References

1. S. Nitopi, E. Bertheussen, S. B. Scott, X. Liu, A. K. Engstfeld, S. Horch, B. Seger, I. E. Stephens, K. Chan and C. Hahn, *Chem. Rev.*, 2019, **119**, 7610–7672.
2. C. Huang and C. Tan, *Aerosol Air Qual Res.*, 2014, **14**, 480–499.
3. X. Wang, Z. Chen, X. Zhao, T. Yao, W. Chen, R. You, C. Zhao, G. Wu, J. Wang and W. Huang, *Angew. Chem. Int. Ed.*, 2018, **57**, 1944–1948.
4. T. Zheng, K. Jiang, N. Ta, Y. Hu, J. Zeng, J. Liu and H. Wang, *Joule.*, 2019, **3**, 265-278.
5. S. Zhang, Z. Xia, Y. Zou, F. Cao, Y. Liu, Y. Ma and Y. Qu, *J. Am. Chem. Soc.*, 2019, **141**, 11353–11357.
6. Y.-J. Zhang, V. Sethuraman, R. Michalsky and A. A. Peterson, *ACS Catal.*, 2014, **4**, 3742–3748.
7. D. Voiry, H. S. Shin, K. P. Loh and M. Chhowalla, *Nat. Rev. Chem.*, 2018, **2**, 0105.
8. H. B. Yang, S.-F. Hung, S. Liu, K. Yuan, S. Miao, L. Zhang, X. Huang, H.-Y. Wang, W. Cai and R. Chen, *Nat. Energy.*, 2018, **3**, 140–147.
9. X. M. Hu, M. H. Rønne, S. U. Pedersen, T. Skrydstrup and K. Daasbjerg, *Angew. Chem. Int. Ed.*, 2017, **56**, 6468–6472.
10. P. T. Smith, B. P. Benke, Z. Cao, Y. Kim, E. M. Nichols, K. Kim and C. J. Chang, *Angew. Chem. Int. Ed.*, 2018, **57**, 9684–9688.
11. M. Zhu, J. Chen, L. Huang, R. Ye, J. Xu and Y. F. Han, *Angew. Chem. Int. Ed.*, 2019, **58**, 6595–6599.
12. S. Lin, C. S. Diercks, Y.-B. Zhang, N. Kornienko, E. M. Nichols, Y. Zhao, A. R. Paris, D. Kim, P. Yang and O. M. Yaghi, *Science*, 2015, **349**, 1208–1213.
13. N. Kornienko, Y. Zhao, C. S. Kley, C. Zhu, D. Kim, S. Lin, C. J. Chang, O. M. Yaghi and P. Yang, *J. Am. Chem. Soc.*, 2015, **137**, 14129–14135.
14. J.-K. Tang, C.-Y. Zhu, T.-W. Jiang, L. Wei, H. Wang, K. Yu, C.-L. Yang, Y.-B. Zhang, C. Chen, Z.-T. Li, D.-W. Zhang and L.-M. Zhang, *J. Mater. Chem. A*, 2020, DOI: 10.1039/D0TA07068H.
15. T. N. Huan, N. Ranjbar, G. Rousse, M. Sougrati, A. Zitolo, V. Mougel, F. Jaouen and M. Fontecave, *ACS Catal.*, 2017, **7**, 1520–1525.
16. Y. Huang, S. Liu, H. Yang, S. Hung, J. Ding, W. Cai, L. Liu, J. Gao, X. Li and T. Zhang, *Angew. Chem. Int. Ed.*, 2019, **59**, 798–803.
17. J. Gu, C.-S. Hsu, L. Bai, H. M. Chen and X. Hu, *Science.*, 2019, **364**, 1091–1094.
18. X.-M. Hu, H. H. Hval, E. T. Bjerglund, K. J. Dalgaard, M. R. Madsen, M.-M. Pohl, E. Welter, P. Lamagni, K. B. Buhl, M. Bremholm, M. Beller, S. U. Pedersen, T. Skrydstrup and K. Daasbjerg, *ACS Catal.*, 2018, **8**, 6255–6264.
19. D. Wang, L. Xiao, P. Yang, Z. Xu, X. Lu, L. Du, O. Levin, L. Ge, X. Pan and J. Zhang, *J. Mater. Chem. A*, 2019, **7**, 11007–11015.
20. C. Andronescu, S. Barwe, E. Ventosa, J. Masa, E. Vasile, B. Konkena, S. Möller and W. Schuhmann, *Angew. Chem. Int. Ed.*, 2017, **56**, 11258–11262.
21. E. A. Mohamed, Z. N. Zahran and Y. Naruta, *Chem. Mater.*, 2017, **29**, 7140–7150.
22. A. Maurin and M. Robert, *Chem. Commun.*, 2016, **52**, 12084–12087.
23. C. Sun, L. Rotundo, C. Garino, L. Nencini, S. S. Yoon, R. Gobetto and C. Nervi, *Chemphyschem.*, 2017, **18**, 3219–3229.
24. X.-M. Hu, S. U. Pedersen and K. Daasbjerg, *Curr Opin Electrochem.*, 2019, **15**, 148–154.
25. H. Yang, Q. Lin, C. Zhang, X. Yu, Z. Cheng, G. Li, Q. Hu, X. Ren, Q. Zhang and J. Liu, *Nat. Commun.*, 2020, **11**, 1–8.
26. S. Tiwari and Bijwe, *Procedia Technology.*, 2014, **14**, 505–512.
27. X. Wang, Z. Chen, X. Zhao, T. Yao, W. Chen, R. You, C. Zhao, G. Wu, J. Wang and W. Huang, *Angew. Chem. Int. Ed.*, 2018, **57**, 1944–1948.

28. S. Lin, C. S. Diercks, Y.-B. Zhang, N. Kornienko, E. M. Nichols, Y. Zhao, A. R. Paris, D. Kim, P. Yang and O. Yaghi, *Science.*, 2015, **349**, 1208–1213.
29. B. Ravel and M. Newville, *J. Synchrotron Radiat.*, 2005, **12**, 537–541.
30. X.-M. Hu, D. Mendoza, M. R. Madsen, D. Joulie, B. Lassalle-Kaiser, M. Robert, S. U. Pedersen, T. Skrydstrup and K. Daasbjerg, *ChemSusChem*, 2020, DOI: 10.1002/cssc.202001311.
31. G. Kresse and J. Furthmüller, *Comput. Mater. Sci.*, 1996, **6**, 15–50.
32. T. Bucko, J. r. Hafner, S. Lebegue and J. G. Angyán, *J. Phys. Chem. A.*, 2010, **114**, 11814–11824.
33. J. P. Perdew, A. Ruzsinszky, G. I. Csonka, O. A. Vydrov, G. E. Scuseria, L. A. Constantin, X. Zhou and K. Burke, *Phys. Rev. Lett.*, 2008, **100**, 136406.
34. A. Roldan, N. Hollingsworth, A. Roffey, H.-U. Islam, J. Goodall, C. Catlow, J. Darr, W. Bras, G. Sankar and K. Holt, *Chem. Commun.*, 2015, **51**, 7501–7504.
35. A. Roldan, *Curr Opin Electrochem.*, 2018, **10**, 1–6.
36. F. Yang, P. Song, X. Liu, B. Mei, W. Xing, Z. Jiang, L. Gu and W. Xu, *Angew. Chem. Int. Ed.*, 2018, **130**, 12483–12487.
37. C. Zhao, X. Dai, T. Yao, W. Chen, X. Wang, J. Wang, J. Yang, S. Wei, Y. Wu and Y. Li, *J. Am. Chem. Soc.*, 2017, **139**, 8078–8081.
38. Y. Mun, S. Lee, K. Kim, S. Kim, S. Lee, J. W. Han and J. Lee, *J. Am. Chem. Soc.*, 2019, **141**, 6254–6262.
39. H. Zhou, T. Liu, X. Zhao, Y. Zhao, H. Lv, S. Fang, X. Wang, F. Zhou, Q. Xu and J. Xu, *Angew. Chem. Int. Ed.*, 2019, **131**, 18559–18564.
40. M. Jia, C. Choi, T.-S. Wu, C. Ma, P. Kang, H. Tao, Q. Fan, S. Hong, S. Liu and Y.-L. Soo, *Chem. Sci.*, 2018, **9**, 8775–8780.
41. Y. Zhang, N. Wang, N. Jia, J. Wang, J. Sun, F. Shi, Z. H. Liu and R. Jiang, *Adv. Mater. Interfaces.*, 2019, **6**, 1900273.
42. C. Hu, S. Bai, L. Gao, S. Liang, J. Yang, S.-D. Cheng, S.-B. Mi and J. Qiu, *ACS Catal.*, 2019, **9**, 11579–11588.
43. C. Lu, J. Yang, S. Wei, S. Bi, Y. Xia, M. Chen, Y. Hou, M. Qiu, C. Yuan, Y. Su, F. Zhang, H. Liang and X. Zhuang, *Adv. Funct. Mater.*, 2019, **29**, 1806884.
44. K. Jiang, S. Siahrostami, T. Zheng, Y. Hu, S. Hwang, E. Stavitski, Y. Peng, J. Dynes, M. Gangisetty and D. Su, *Energy Environ. Sci.*, 2018, **11**, 893–903.
45. X. Rong, H. J. Wang, X. L. Lu, R. Si and T. B. Lu, *Angew. Chem. Int. Ed.*, 2019, **59**, 1961–1965.
46. E. Zhang, T. Wang, K. Yu, J. Liu, W. Chen, A. Li, H. Rong, R. Lin, S. Ji, X. Zheng, Y. Wang, L. Zheng, C. Chen, D. Wang, J. Zhang and Y. Li, *J. Am. Chem. Soc.*, 2019, **141**, 16569–16573.
47. H. Shang, T. Wang, J. Pei, Z. Jiang, D. Zhou, Y. Wang, H. Li, J. Dong, Z. Zhuang, W. Chen, D. Wang, J. Zhang and Y. Li, *Angew. Chem. Int. Ed.*, 2020, DOI: 10.1002/anie.202010903.
48. F. Sanchez, D. Motta, A. Roldan, C. Hammond, A. Villa and N. Dimitratos, *Top Catal.*, 2018, **61**, 254–266.
49. Y. Lei, Y. Wang, Y. Liu, C. Song, Q. Li, D. Wang and Y. Li, *Angew. Chem. Int. Ed.*, 2020, DOI: 10.1002/ange.201914647.
50. M. D. Hossain, Z. Liu, M. Zhuang, X. Yan, G. L. Xu, C. A. Gadre, A. Tyagi, I. H. Abidi, C. J. Sun and H. Wong, *Adv. Energy Mater.*, 2019, **9**, 1803689.
51. J. Conesa and Font, *Polym. Eng. Sci.*, 2001, **41**, 2137–2147.
52. N. Elgrishi, S. Griveau, M. B. Chambers, F. Bedioui and M. Fontecave, *Chem. Commun.*, 2015, **51**, 2995–2998.
53. A. Maurin and M. Robert, *Chem. Commun.*, 2016, **52**, 12084–12087.
54. A. Zhanaidarova, C. E. Moore, M. Gembicky and C. P. J. C. C. Kubiak, *Chem. Commun.*, 2018, **54**, 4116–4119.
55. Y. Wang, S. L. Marquard, D. Wang, C. Dares and T. J. Meyer, *ACS Energy Lett.*, 2017, **2**, 1395–1399.
56. A. N. Marianov and Y. Jiang, *Appl. Catal. B.*, 2019, **244**, 881–888.
57. Q. Fan, P. Hou, C. Choi, T. S. Wu, S. Hong, F. Li, Y. L. Soo, P. Kang, Y. Jung and Z. Sun, *Adv. Energy Mater.*, 2020, **10**, 1903068.
58. F. Pan, H. Zhang, Z. Liu, D. Cullen, K. Liu, K. More, G. Wu, G. Wang and Y. Li, *J. Mater. Chem. A.*, 2019, **7**, 26231–26237.
59. H. Yang, Q. Lin, C. Zhang, X. Yu, Z. Cheng, G. Li, Q. Hu, X. Ren, Q. Zhang, J. Liu and C. He, *Nat. Commun.*, 2020, **11**, 593.
60. W. Ren, X. Tan, X. Chen, G. Zhang, K. Zhao, W. Yang, C. Jia, Y. Zhao, S. C. Smith and C. Zhao, *ACS Catal.*, 2020, **10**, 13171–13178.